

Universal properties and structure of halo nuclei

David L. Canham^{1,a} and H.-W. Hammer^{1,2,b}

¹ Helmholtz-Institut für Strahlen- und Kernphysik (Theorie), Universität Bonn, 53115 Bonn, Germany

² Bethe Center for Theoretical Physics, Universität Bonn, 53115 Bonn, Germany

Received: 24 July 2008

Published online: 28 August 2008 – © Società Italiana di Fisica / Springer-Verlag 2008

Communicated by J. Wambach

Abstract. The universal properties and structure of halo nuclei composed of two neutrons ($2n$) and a core are investigated within an effective quantum mechanics framework. We construct an effective interaction potential that exploits the separation of scales in halo nuclei and treat the nucleus as an effective three-body system. The uncertainty from higher orders in the expansion is quantified through theoretical error bands. First, we investigate the possibility to observe excited Efimov states in $2n$ halo nuclei. Based on the experimental data, ^{20}C is the only halo nucleus candidate to possibly have an Efimov excited state, with an energy less than 7 keV below the scattering threshold. Second, we study the structure of ^{20}C and other $2n$ halo nuclei. In particular, we calculate their matter form factors, radii, and two-neutron opening angles.

PACS. 21.45.-v Few-body systems – 21.60.Gx Cluster models – 21.10.Gv Nucleon distributions and halo features – 21.30.Fe Forces in hadronic systems and effective interactions

1 Introduction

There has been a considerable interest in physical systems with large scattering lengths recently. The scattering of two particles with short-range interactions at sufficiently low energy is determined by their S -wave scattering length a . If a is much larger than the range of the interaction r_0 , the system shows universal properties [1]. The simplest example is the existence of a shallow two-body bound state if a is large and positive, but there are many more, including the effects of a limit cycle [2] and the Efimov effect [3] in the three-body system.

The best-known example of a nuclear system with a large scattering length is the two-nucleon (NN) system. There are two independent S -wave scattering lengths that govern the low-energy scattering of nucleons. Both scattering lengths are significantly larger than the range of the interaction $r_0 \sim 1/m_\pi \approx 1.4$ fm, while the effective ranges are of the same order as r_0 . As a consequence, the description of few-nucleon systems in an expansion in $r_0/|a|$ is useful. It has successfully been applied to various two-, three-, and four-nucleon observables (see refs. [4–6] and references therein).

Another type of system that can be described with these techniques are halo nuclei: a special class of nuclear

systems which offer the possibility of exploring universal behavior [7–11]. Halo nuclei consist of a tightly bound core and a “halo” of lightly bound nucleons. They are characterized by their large nuclear radius compared to the radius of the core. Equivalently, the separation energy of the halo nucleons is small compared to the excitation energy of the core. This separation of scales allows for the use of effective theories, where one can assume the core to be a structureless particle, and treat the nucleus as a few-body system of the core and the valence nucleons.

The first application of effective field theory methods to halo nuclei was carried out in refs. [12,13], where the neutron-alpha system (“ ^5He ”) was considered. More recent studies have focused on the consistent inclusion of the Coulomb interaction in two-body halo nuclei such as the proton-alpha [14] and alpha-alpha systems [15]. Three-body halo nuclei composed of a core and two valence neutrons are of particular interest due to the possibility of these systems to display the Efimov effect [3]. Efimov found that in three-body systems of non-relativistic particles, if at least two of the three pairs of particles have a large scattering length $|a|$ compared to the range r_0 of the interaction, there occurs a sequence of three-body bound states whose binding energies are spaced geometrically between \hbar^2/mr_0^2 and \hbar^2/ma^2 . The number of bound states grows to infinity, with an accumulation point at the three-body scattering threshold, in the limit $\pm a \rightarrow \infty$. The se-

^a e-mail: canham@itkp.uni-bonn.de

^b e-mail: hammer@itkp.uni-bonn.de

quence of three-body bound states has universal properties that are independent of the details of the two-body potential at short distances. The influence of long-range Coulomb interactions on the geometric bound state spectrum was recently investigated in a model study [16].

The first experimental evidence for Efimov states in ultracold Cs atoms has recently been found through their signature in three-body recombination rates [17]. This signature could be unravelled by varying the scattering length a over several orders of magnitude using a Feshbach resonance. For halo nuclei, the interaction strength cannot easily be varied and one has to look for different signatures of the Efimov effect. Since the ground state of a halo nucleus cannot be uniquely identified as an Efimov state for fixed a , it is customary to look for excited states that have the Efimov character. One can then consider a halo nucleus to display the Efimov effect if it has at least one excited state with universal properties.

In this paper, we explore the occurrence of the Efimov effect and its well-known universal properties for $2n$ halo nuclei with a core of spin zero. From the earliest studies of halo nuclei, ^{20}C has been suggested as a good candidate for Efimov states [18], with future theoretical work supporting this prediction [19,20]. We critically examine these earlier studies and perform an improved analysis in the framework of an effective theory. The uncertainties of our leading-order analysis are quantified through error bands. In the second part of this paper, we focus on the structure of $2n$ halo nuclei. In particular, we calculate their matter form factors, radii, and two-neutron opening angles. Finally, we end with conclusions and an outlook.

2 Theoretical framework

For our study, we choose the effective quantum mechanics framework of refs. [6,21,22] which is equivalent to using field-theoretic language for the problem at hand. The short-range interactions characteristic of halo nuclei are then described using an effective interaction potential. The low-energy behavior of the system can then be reproduced with a level of accuracy proportional to powers of the low-momentum scale M_{low} over the high-momentum scale M_{high} . The theory is valid up to a momentum, M_{high} , at which the errors become of order one. For example, the two-body interactions of halo nuclei can be characterized by their large scattering lengths, $a \sim 1/M_{low}$, and their range, $r_0 \sim 1/M_{high}$. Such systems need to leading order one coupling parameter, C_0 , for each pair interaction tuned to reproduce the scattering length. The range of the interaction enters at next-to-leading order. For $a > 0$, there is a two-body bound state, and the binding energy can then be found through the universal formula:

$$B_2 = \frac{\hbar^2}{2\mu a^2} + \dots, \quad (1)$$

where μ is the reduced mass. The dots indicate corrections of the order $\sqrt{2\mu B_2}/M_{high} \sim r_0/a$.

For the large separation of scales involved in halo nuclei, zero-range interactions can be used in constructing the effective interaction potential. This leads to a separable potential made up of contact interactions in a momentum expansion. The 2-body S -wave potential to leading order is

$$\langle \mathbf{p} | V_{eff} | \mathbf{p}' \rangle = C_0 g(p)g(p') + \dots, \quad (2)$$

where the dots indicate higher-order momentum dependent interactions which we will neglect. In a future study, the errors could be systematically reduced by including the effective range correction to eq. (2). $g(p)$ is the regulator function (sometimes called the form factor) of the theory. Of course, the low-energy observables must be independent of the regularization scheme, and one can choose the scheme most convenient for calculations. We use a momentum cutoff scheme, multiplying the coupling parameter with a Gaussian regulator function

$$g(p) = \exp\left(-\frac{p^2}{\Lambda^2}\right), \quad (3)$$

where Λ is the cutoff parameter. This regulator function obviously suppresses the contributions of momenta $p, p' \gg \Lambda$, where the effective potential would break down and no longer be valid. A natural choice for the value of Λ is therefore $\Lambda \sim M_{high}$, but observables are independent of Λ after renormalization.

This potential is then used in the solution of the three-body Faddeev equations in terms of the spectator functions $F_i(q)$, which represent the dynamics of the core ($i = c$) and the halo neutron ($i = n$). To find the bound state of a halo nucleus composed of two valence neutrons and a core with spin zero, the resulting coupled integral equations are simply a generalization of the three-boson equation¹ (see [21] and references within). We use units such that $\hbar = c = 1$ and the nucleon mass $m = 1$:

$$F_n(q) = \frac{1}{2} \int_0^\infty dq' q'^2 \int_{-1}^1 dx [g(\tilde{\pi}(q, q'))g(\tilde{\pi}(q', q)) \times G_0^n(\tilde{\pi}(q', q), q'; B_3)t_n(q'; B_3)F_n(q') + g(\tilde{\pi}_1(q, q'))g(\tilde{\pi}_2(q, q')) \times G_0^c(\tilde{\pi}_2(q, q'), q'; B_3)t_c(q'; B_3)F_c(q')], \quad (4)$$

$$F_c(q) = \int_0^\infty dq' q'^2 \int_{-1}^1 dx [g(\tilde{\pi}_1(q', q))g(\tilde{\pi}_2(q', q)) \times G_0^n(\tilde{\pi}_1(q', q), q'; B_3)t_n(q'; B_3)F_n(q')], \quad (5)$$

where the shifted momenta $\tilde{\pi}$, $\tilde{\pi}_1$, and $\tilde{\pi}_2$ are given by

$$\tilde{\pi}(q, q') = \sqrt{\left(\frac{1}{A+1}\right)^2 q^2 + q'^2 + \frac{2}{A+1} qq'x}, \quad (6)$$

$$\tilde{\pi}_1(q, q') = \sqrt{\left(\frac{A}{A+1}\right)^2 q^2 + q'^2 + \frac{2A}{A+1} qq'x}, \quad (7)$$

¹ In fact, the equations are the same for any bound three-body system of two identical particles and a core with spin zero, which interact through the pair-wise zero-range potentials given in eq. (2).

and

$$\tilde{\pi}_2(q, q') = \sqrt{q^2 + \frac{1}{4}q'^2 + qq'x}. \quad (8)$$

In the above equations, $B_3 > 0$ is the three-body bound-state energy and A is the number of nucleons in the core. The free three-body propagators for a spectator neutron G_0^n and a spectator core G_0^c are

$$G_0^n(p, q; B_3) = \left[B_3 + \frac{A+1}{2A}p^2 + \frac{A+2}{2(A+1)}q^2 \right]^{-1}, \quad (9)$$

$$G_0^c(p, q; B_3) = \left[B_3 + p^2 + \frac{A+2}{4A}q^2 \right]^{-1}. \quad (10)$$

The effects of the interactions are contained in the two-body T -matrices which are obtained by solving the Lippmann-Schwinger equation for the neutron-neutron and neutron-core interaction with the effective potential, eq. (2). In the kinematics of eqs. (4), (5), we have

$$\begin{aligned} t_n(q'; B_3) &= \frac{1}{\pi} \frac{A+1}{A} \left[-\frac{1}{a_{nc}} \exp(2/(a_{nc}^2 \Lambda^2)) \right. \\ &\quad \times \operatorname{erfc}(\sqrt{2}/(|a_{nc}| \Lambda)) \\ &\quad + \sqrt{\tilde{E}_n(q'; B_3)} \exp(2\tilde{E}_n(q'; B_3)/\Lambda^2) \\ &\quad \left. \times \operatorname{erfc}(\sqrt{2\tilde{E}_n(q'; B_3)}/\Lambda) \right]^{-1}, \end{aligned} \quad (11)$$

with

$$\tilde{E}_n(q'; B_3) = \frac{2A}{A+1} \left(B_3 + \frac{A+2}{2(A+1)}q'^2 \right), \quad (12)$$

and

$$\begin{aligned} t_c(q'; B_3) &= \frac{2}{\pi} \left[-\frac{1}{a_{nn}} \exp(2/(a_{nn}^2 \Lambda^2)) \right. \\ &\quad \times \operatorname{erfc}(\sqrt{2}/(|a_{nn}| \Lambda)) \\ &\quad + \sqrt{\tilde{E}_c(q'; B_3)} \exp(2\tilde{E}_c(q'; B_3)/\Lambda^2) \\ &\quad \left. \times \operatorname{erfc}(\sqrt{2\tilde{E}_c(q'; B_3)}/\Lambda) \right]^{-1}, \end{aligned} \quad (13)$$

with

$$\tilde{E}_c(q'; E) = B_3 + \frac{A+2}{4A}q'^2, \quad (14)$$

where the indices n, c indicate the spectator particle. In eqs. (11), (13), $\operatorname{erfc}(x) = 1 - (2/\sqrt{\pi}) \int_0^x \exp(-t^2) dt$ denotes the complementary error function, which will go quickly to 1 for $x \ll 1$. If the cutoff is chosen large compared to all momentum scales involved in the problem: $\Lambda \gg 1/|a|, \sqrt{\tilde{E}}$, these T -matrices reproduce the usual effective range expansion at leading order.

A two-body bound state appears as a simple pole in the two-body t -matrix at an energy $E = -B_2$. In our renormalization of the coupling parameter, we have tuned

$C_0(\Lambda)$ so that it reproduces the scattering length needed to produce this two-body binding energy to leading order, as given in eq. (1):

$$\frac{1}{C_0} = 2\pi^2 2\mu \left[\frac{1}{a} \exp\left(\frac{2}{a^2 \Lambda^2}\right) \operatorname{erfc}\left(\frac{\sqrt{2}}{|a|\Lambda}\right) - \frac{\Lambda}{2} \sqrt{\frac{2}{\pi}} \right]. \quad (15)$$

This renormalization works equally well for the case of virtual states, $a < 0$. Also, for $\Lambda \gg 1/|a|$, the exp and erfc functions both quickly approach 1, and the resulting relations are analogous to ref. [1].

For most halo nuclei, the S -wave scattering length is not as well known as the two-body bound (virtual) state energy. Therefore, we will generally use the two-body energies, E_{nn} and E_{nc} , as input parameters, from which we can calculate the scattering length to leading order through eq. (1), $1/a_{ni} = \pm \sqrt{2\mu_{ni} E_{ni}}$, where the $+$ refers to a bound state and the $-$ to a virtual state, $i = n$ or c , and μ_{ni} is the corresponding reduced mass. The difference between the two-body energy and the S -wave scattering length is higher order in the expansion in $M_{low}/M_{high} \sim r_0/|a|$.

3 Universal properties

3.1 The Efimov effect in 2n halo nuclei

The three-body binding energies are given by the values of B_3 for which the coupled integral equations, eqs. (4), (5), have a nontrivial solution. In principle, eqs. (4), (5), should also include a three-body force term which is required for proper renormalization. However, due to the limit cycle behavior of this three-body force, it is always possible to choose a cutoff where the three-body force vanishes. As a consequence, we can simply drop the three-body force and work with a finite cutoff Λ as in ref. [21]. Tuning this cutoff to reproduce a given three-body observable, we can predict other low-energy observables by using the same cutoff [1, 23]. The cutoff is inversely related to the interaction radius (see [24] and references within), thus taking the cutoff to infinity is equivalent to taking the range of our potential to zero. It is at this limit that the Thomas collapse [25] will occur and the energy of the three-body ground state will diverge.

The Thomas collapse is closely related to the Efimov effect in that the deepest three-body bound states of the Thomas collapse can be identified with the deepest Efimov states [26]. The sequence of three-body Efimov states can be found from our integral equations with sufficiently large scattering lengths by finding the spectrum of binding energies for a fixed cutoff. By increasing the cutoff new three-body bound states appear in the spectrum at critical values of Λ , which are geometrically separated. Accordingly, the energies of the deeper bound states increase in magnitude. The Thomas effect is seen by the divergence of the deepest bound-state energy for $\Lambda \rightarrow \infty$. However,

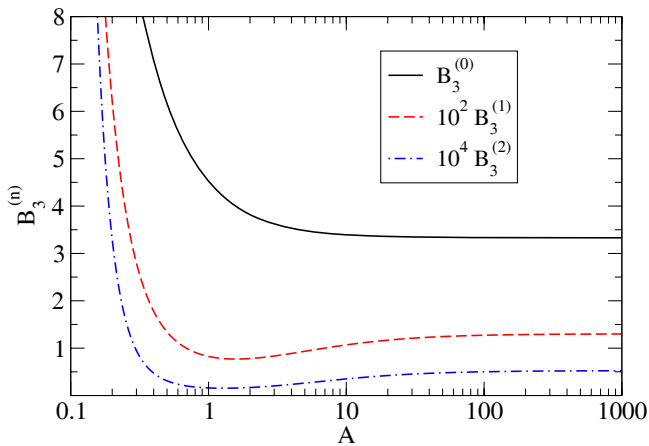


Fig. 1. Spectrum of three-body bound states, when two of the particles have equal mass $m_1 = m_2$, as a function of the mass ratio, $A = m_3/m_1$, in the resonant limit $a \rightarrow \pm\infty$. The cutoff parameter was fixed at a value of $\Lambda = 10.0$ (the units of Λ and $B_3^{(n)}$ are arbitrary, for details see text).

the states below the natural cutoff, $1/(m\kappa_0^2)$, are physically irrelevant. They are outside the range of validity of the effective theory and can be ignored.

Conversely, the sequence of three-body Efimov states have universal properties that are insensitive to the details of the two-body potential at short distances, and hence independent of the cutoff. One such property is that for the resonant limit, $a \rightarrow \pm\infty$, at which there are infinitely many arbitrarily shallow three-body bound states, the ratio of the binding energies of neighboring bound states approaches a universal factor, λ_0 , as the threshold is approached:

$$B_3^{(n)}/B_3^{(n+1)} \longrightarrow (\lambda_0)^2, \quad (16)$$

as $n \rightarrow +\infty$ with $a = \pm\infty$. This universal scaling factor λ_0 depends on the masses of the particles. In our case, the masses of the two neutrons are equal, $m_1 = m_2$, and the core mass $A = m_3/m_1$. The values of $B_3^{(n)}$ for $n = 1, 2, 3$ as a function of the core mass A are shown in fig. 1 for a finite value of $\Lambda = 10$. Note that because we have taken $a \rightarrow \pm\infty$, Λ is given in units of an arbitrary momentum scale κ . All energies are then given in units of κ^2 . One interesting feature is the appearance of a minimum in the binding energy. The absence of this minimum in the $B_3^{(0)}$ curve is due to the fact that the magnitude of $B_3^{(0)}$ is near the order of magnitude of A , and details of the regularization scheme become important. Also, we see that the binding energy quickly reaches an asymptotic value for very large A , and diverges for $A \rightarrow 0$. The dependence of the discrete scaling factor, λ_0 , on the core mass A is well known (see, *e.g.*, the review [1], fig. 52). We have checked our code by reproducing these results. In particular, the discrete scaling factor is largest for all equal masses, where it has the same value $\lambda_0 \approx 22.7$ as for three identical bosons. In the very large core limit, $A \gg 1$, the discrete scaling factor approaches 15.7. In the vanishing core limit, $A \ll 1$, it approaches 1 as all three-body binding energies diverge.

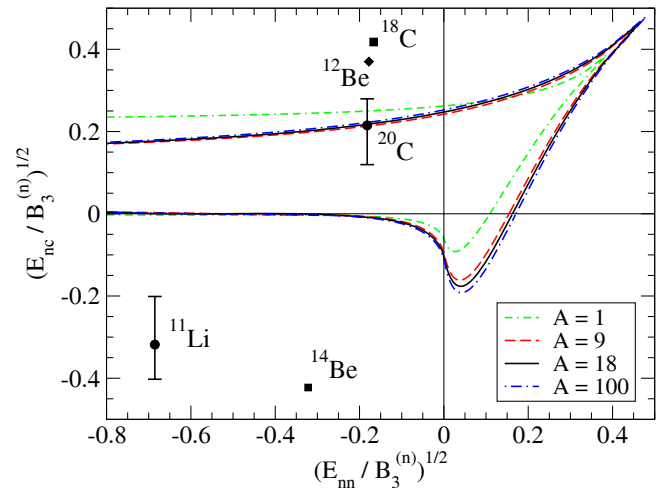


Fig. 2. Boundary curves in the $\sqrt{E_{nc}/B_3^{(n)}}$ vs. $\sqrt{E_{nn}/B_3^{(n)}}$ plane, where the binding energy of the excited Efimov state $B_3^{(n+1)}$ is exactly at threshold. Negative values on the axes correspond to virtual two-body states. Boundary curves are shown for various core masses $A = 1, 9, 18$, and 100 . Experimental data shown for ^{20}C , ^{18}C , ^{11}Li , ^{12}Be , and ^{14}Be are taken from ref. [30].

3.2 Possibility of Efimov excited states in 2n halo nuclei

Our main aim in this section is to assess which halo nuclei have the possibility of possessing an excited Efimov state. The ground-state energy and the two-body energies cannot be predicted by our theory and are taken from experiment. In other words, we would generally like to know what the values of the two-body energies must be, or correspondingly how large the scattering lengths must be, in order to produce an excited Efimov state, knowing the ground-state binding energy.

To this end, we construct the parametric region defined by the ratios, $\sqrt{E_{nc}/B_3^{(n)}}$ vs. $\sqrt{E_{nn}/B_3^{(n)}}$. The boundary curves representing the existence of an excited Efimov state for various values of the core mass are shown in fig. 2. An analogous study was carried out in ref. [19] (see below). All points which lie within the boundary curve have at least one excited Efimov state above the state with energy $B_3^{(n)}$, while the points outside the curve have no excited states above this state. The curve itself is built up of the points for which the $B_3^{(n+1)}$ binding energy is equal to the scattering threshold; *i.e.* $B_3^{(n+1)} = E_{ni}$ for E_{nn} or E_{nc} bound, where E_{ni} is the larger of E_{nn} and E_{nc} , and $B_3^{(n+1)} = 0$ for E_{nn} and E_{nc} virtual. The boundary curves in fig. 2 were found with $n = 1$ in order to minimize the regulator effects. Due to the scaling symmetry of the sequence of three-body bound states, the n -th state can always be interpreted as the ground state and the $(n+1)$ -th state as the first excited state².

² Because of the regulator effects, the curves found with $n = 0$ are slightly different from the curves in fig. 2. The curves are practically the same for larger values of n , as the numerical values of $B_3^{(n)}$ are much smaller than the cutoff Λ for $n > 0$.

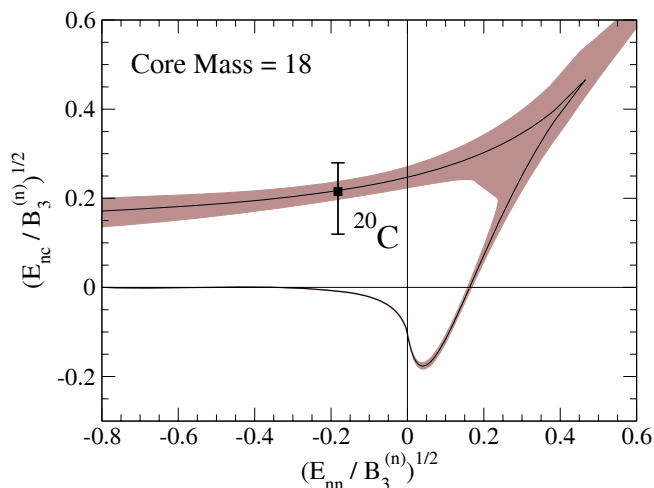


Fig. 3. Boundary curve in the $\sqrt{E_{nc}/B_3^{(n)}}$ vs. $\sqrt{E_{nn}/B_3^{(n)}}$ plane with leading-order error bands. The boundary curve is shown for a core mass of $A = 18$ with the experimental data for ^{20}C from ref. [30].

Here it is of interest to note that these results differ from the results found by Amorim *et al.* in an analogous study [19] using a hard momentum cutoff rather than the Gaussian regulator scheme. We found that the results agree almost exactly for a core mass equal to the nucleon mass, $A = 1$, but differ significantly for all other values of the core mass. While the qualitative conclusions on the likelihood of Efimov states in $2n$ halo nuclei are the same, the quantitative results are different. In fact, in doing the numerical calculations with a hard cutoff ourselves, we found results that match those presented here.

These results represent the leading-order calculations with the effective potential described in eq. (2). The theoretical uncertainty in calculating the binding energy is of the order $\approx r_0/a$, where r_0 is the effective range of the potential, and a is the scattering length. As stated before, the cutoff parameter is related to the inverse of the range of the potential, such that we can approximate $r_0 \approx 1/\Lambda$. However, it is important in this error estimate that the Λ used comes from the result with $n = 0$, the true ground state, rather than $n = 1$. This corresponds to taking the “natural” value for the cutoff Λ . We therefore estimate the leading fractional error of our boundary curves as $\approx \sqrt{2\mu_{ni}E_{ni}}/\Lambda$, for $i = n$ and c , respectively. The resulting boundary curve including leading-order error bands, using the case of core mass $A = 18$ is shown in fig. 3. This graph is a good representation of the error bands for other core masses. The uncertainty of our leading-order calculation becomes large for values of $\sqrt{E_{nn}/B_3^{(n)}} + E_{nc}/B_3^{(n)}$ near 1 and greater. At this point the low-energy observables approach the order of magnitude of Λ , where the effective potential is no longer a good description of the three-body system.

Now we discuss the implications of figs. 2 and 3 for the existence of excited Efimov states in halo nuclei in more detail. The four quadrants of the parametric plane in these

figures correspond to the four different types of three-body halo nuclei, determined by the different types of two-body subsystems. The upper-right quadrant corresponds to both the n - n and the n - c subsystems being bound, and is accordingly called *All Bound*. The lower-right quadrant is that in which the n - n subsystem is bound, but the n - c subsystem is unbound, and receives the name *Tango* [27]. Of course, because we are concerned with $2n$ halo nuclei, where the n particle is truly a neutron, these two quadrants are not of much interest in the present study. The upper-left quadrant corresponds to the unbound n - n subsystem with a bound n - c subsystem, for which we use the name *Samba* as recommended in [28]. The final quadrant corresponds to the three-body systems for which none of the two-body subsystems is bound. This system is referred to as a *Borromean* system.

We can now use our plot to analyze the likelihood of the Efimov effect for the different types of three-body systems, with a focus on $2n$ halo nuclei. As one would expect, the *Borromean* systems offer the smallest chance of having an excited Efimov state, as the two-body energy would have to be very small, or accordingly the scattering length very large, to produce even one excited state. However, this can be achieved in ultra-cold atoms, as the presence of the so-called *Feshbach resonances* allows one to tune the two-body scattering length to a very large value [29]. Interestingly, the *Samba* systems have the largest region supporting the occurrence of excited Efimov states. As long as the n - c scattering length is large enough, there can be a large variation in the n - n scattering length that would still allow for the Efimov effect. This agrees with the findings of Efimov [3], that as long as 2 of the 3 two-body interactions have a large scattering length, the sequence of three-body binding energies can occur.

Looking at possible halo nuclei candidates, we have plotted the positions of ^{20}C , ^{18}C , ^{11}Li , ^{12}Be , and ^{14}Be in fig. 2, using the experimental values of the “Nuclear Data Evaluation Project” of TUNL [30] for the n - c and three-body ground-state energy data, and the standard value of the n - n scattering length, $a_{nn} = (-18.7 \pm 0.6)$ fm [31] to calculate the n - n two-body energy according to eq. (1). The only halo candidate that has any possibility of an excited Efimov state is ^{20}C , due to the large uncertainty in the n - ^{18}C bound-state energy. We will return to this nucleus shortly. The positions and relatively small experimental errors in the other halo nuclei data rule out the chance of finding excited Efimov states in these nuclei. Other halo nuclei candidates which exist have values of the two-body energies which are too large to even appear on our plot.

3.3 Efimov excited state for ^{20}C

The central value for the n - ^{18}C bound state energy, $E_{nc} = (162 \pm 112)$ keV [32], lies almost exactly on the boundary region for $A = 18$ in fig. 3. The large error in this value, however, dips well into the region where at least one excited Efimov state can occur. The error in the three-body ground-state energy of ^{20}C is small compared to E_{nc} .

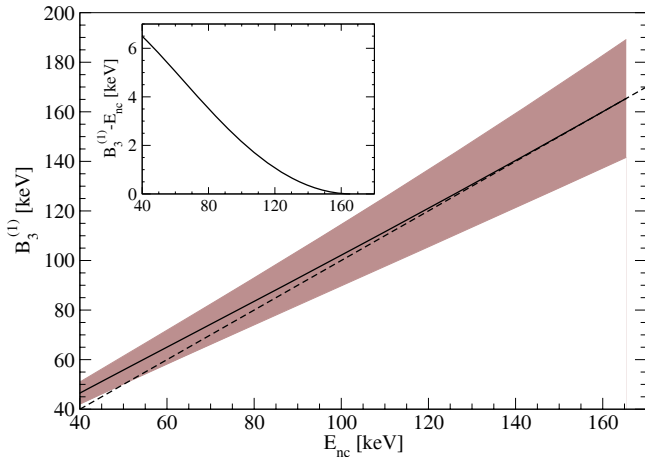


Fig. 4. Binding energy of the ^{20}C excited Efimov state as a function of the $n\text{-}^{18}\text{C}$ bound-state energy (solid line) with leading-order error bands. The dashed line represents the scattering threshold which is given by $B_3^{(1)} = E_{nc}$. The inset shows the excited state energy relative to the scattering threshold.

Thus, we can calculate the value of the excited state energies as a function of E_{nc} , using the standard value for a_{nn} , and fixing our cutoff to reproduce the experimental value of the ground-state energy $B_3^{(0)} = 3506.0$ keV [30,32]. The result is plotted in fig. 4, where the solid line is the excited state energy, and the dashed line represents the scattering threshold. The inset graph shows the excited state energy relative to the scattering threshold. We find only one excited Efimov state, existing when $E_{nc} < 165$ keV. For larger values of E_{nc} , the ^{20}C system moves outside of the boundary curve, and the excited Efimov state is destroyed. The binding energy relative to the scattering threshold is always below 7 keV, a value very small in comparison with the ground-state energy. Also, the error bands are large compared to the relative energy of the excited state to the scattering threshold, with the lower error band almost always below the scattering threshold.

We have again estimated this error using the theoretical uncertainty of our effective potential. In this first-order calculation, the uncertainty in binding energies calculated using the two-body effective potential of eq. (2) is $\approx r_0/a$. Our effective potential, made up of contact interactions, will break down for momenta of the order of the pion mass $m_\pi = 140$ MeV to estimate the effective range $r_0 \approx 1/m_\pi$. The uncertainty in the binding energy of the excited state is then the quadratic sum of the uncertainties from the $n\text{-}n$ and $n\text{-}^{18}\text{C}$ interactions: $\sqrt{2\mu_{nn}E_{nn}/m_\pi^2 + 2\mu_{nc}E_{nc}/m_\pi^2}$. These uncertainties are of the same order of magnitude as those found assuming that the effective range is related to the inverse of the cutoff, $r_0 \approx 1/\Lambda$.

This result is in overall qualitative agreement with the previous studies of Amorim *et al.* [19] and Mazumdar *et al.* [20], who also found the presence of a very weakly bound excited Efimov state in ^{20}C for sufficiently small values of E_{nc} . However, both of these studies have a larger value for the excited state energy, with the

Mazumdar group also finding a second excited state for $E_{nc} < 100$ keV. Also, the disagreement with the results of the Amorim paper mentioned before casts doubts on the quantitative results of [19], as a more recent study from the same group [33] suggests better agreement with the results presented here. This newer analysis is one of a few recent studies extending the trajectory of this excited state into the scattering region to explore the possibility of finding a resonance in the $n\text{-}^{19}\text{C}$ scattering sector [33–35].

4 Form factors and mean square radii

We are now interested in calculating other low-energy physical properties of three-body halo nuclei, specifically the matter density form factors and the mean square radii. The information needed to calculate such quantities is held in the wave functions of the known bound states. In the previous sections, we only required the Faddeev spectator functions F_n and F_c . However, the full three-body wave function can be reconstructed from the Faddeev spectator functions (see appendix A for details). Once the three-body wave function is known, the corresponding one- and two-body matter density form factors can be computed. Finally, the mean square distances between two of the three particles as well as the mean square distance of one of the particles from the center of mass can be extracted from the proper form factor.

4.1 One- and two-body matter density form factors

The three-body wave functions found in appendix A can be used to calculate other low-energy properties of the three-body bound state. With the Jacobi momentum states it is straightforward to calculate the Fourier transform of the one- and two-body matter densities with respect to the momentum transfer squared. These are defined as the one- and two-body matter density form factors, $\mathcal{F}_i(k^2)$ and $\mathcal{F}_{ni}(k^2)$ respectively, where $i = n, c$. In the wave functions, the \mathbf{p} Jacobi momentum describes the relative momentum between the two particles in the chosen two-body subsystem, while \mathbf{q} describes the momentum of the spectator particle relative to the center of mass of the two-body subsystem³. Therefore, the one-body form factors can be obtained as follows:

$$\mathcal{F}_i(k^2) = \int d^3p d^3q \Psi_i(\mathbf{p}, \mathbf{q}) \Psi_i(\mathbf{p}, \mathbf{q} - \mathbf{k}), \quad (17)$$

where $i = n, c$ depending on the desired two-body subsystem. The two-body form factors can be solved similarly:

$$\mathcal{F}_{nc}(k^2) = \int d^3p d^3q \Psi_n(\mathbf{p}, \mathbf{q}) \Psi_n(\mathbf{p} - \mathbf{k}, \mathbf{q}), \quad (18)$$

and

$$\mathcal{F}_{nn}(k^2) = \int d^3p d^3q \Psi_c(\mathbf{p}, \mathbf{q}) \Psi_c(\mathbf{p} - \mathbf{k}, \mathbf{q}). \quad (19)$$

³ Recall that we use the spectator notation for the wave functions, where the index i on Ψ_i refers to the spectator particle.

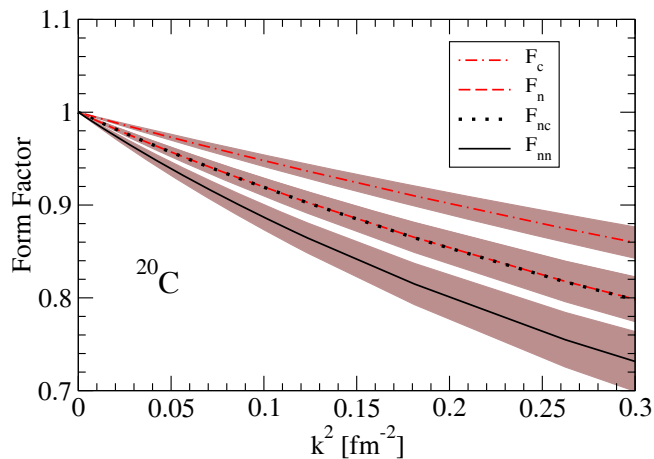


Fig. 5. The various one- and two-body matter density form factors with leading-order error bands for the ground state of ^{20}C in the low-energy region: $\mathcal{F}_{nn}(k^2)$ black solid line; $\mathcal{F}_{nc}(k^2)$ black dotted line; $\mathcal{F}_n(k^2)$ lighter (red on-line) dashed line; $\mathcal{F}_c(k^2)$ lighter (red on-line) dot-dashed line.

These relations can be simplified further by using the fact that at leading order only S -waves contribute. Consequently, we project the three-body wave functions onto the S -wave, and then perform the angular integrations. In our normalization, the wave functions then obey the relation:

$$\Psi_i(p, q) = 4\pi \langle \Psi_i(\mathbf{p}, \mathbf{q}) \rangle, \quad (20)$$

where $\langle \dots \rangle$ denotes the angular average. This relation is then substituted into the above form factor relations, and the trivial angular integrations can be performed. Furthermore, the form factors will be normalized in the end such that $\mathcal{F}(k^2 = 0) = 1$, so any constant overall factor can be dropped. For the one-body form factors we have

$$\begin{aligned} \mathcal{F}_i(k^2) &= \int dp p^2 \int dq q^2 \int_{-1}^1 dx \Psi_i(p, q) \\ &\quad \times \Psi_i(p, \sqrt{q^2 + k^2 - 2qkx}), \end{aligned} \quad (21)$$

and for the two-body form factors we have

$$\begin{aligned} \mathcal{F}_{nc}(k^2) &= \int dp p^2 \int dq q^2 \int_{-1}^1 dx \Psi_n(p, q) \\ &\quad \times \Psi_n(\sqrt{p^2 + k^2 - 2pkx}, q), \end{aligned} \quad (22)$$

and

$$\begin{aligned} \mathcal{F}_{nn}(k^2) &= \int dp p^2 \int dq q^2 \int_{-1}^1 dx \Psi_c(p, q) \\ &\quad \times \Psi_c(\sqrt{p^2 + k^2 - 2pkx}, q). \end{aligned} \quad (23)$$

The expressions relating $\Psi_n(p, q)$ and $\Psi_c(p, q)$ to the solutions $F_n(q)$ and $F_c(q)$ of eqs. (4), (5) are given in appendix A. We are now in the position to calculate these form factors for halo nuclei.

As a general example, we have plotted the form factors for the ground state of ^{20}C , in the low-energy region

in fig. 5, using a bound-state energy of 3506.0 keV, a n - n two-body virtual energy of 116.04 keV, and a n - c bound-state energy of 161.0 keV. The theory breaks down for momentum transfers of the order of the pion mass squared ($k^2 \approx 0.5 \text{ fm}^{-2}$) where the one-pion exchange interaction cannot be approximated by short-range contact interactions anymore. Here one can see that for low momentum transfer the one-body neutron, $\mathcal{F}_n(k^2)$, and the two-body core-neutron, $\mathcal{F}_{nc}(k^2)$, form factors lie nearly on top of each other. This is due to the fact that the core consists of 18 nucleons and, therefore, the center of mass is very near the core. This fact is also seen in the shallow slope of the one-body core form factor, $\mathcal{F}_c(k^2)$.

The theoretical error bands in the form factors are an estimate arising from the theoretical uncertainty of our two-body effective potential, eq. (2). In this first-order calculation, the uncertainty in the effective potential comes from the next term in the expansion, which is related to the effective range. Therefore, the theoretical uncertainty is $\approx r_0/a$. As discussed above, we use the inverse of the pion mass $m_\pi = 140 \text{ MeV}$ to approximate the effective range, $r_0 \approx 1/m_\pi$. With the form factors normalized to $\mathcal{F}(k^2 = 0) = 1$, and because $|E_{nc}| > |E_{nn}|$, the theory error is estimated to be $\approx (1 - \mathcal{F})\sqrt{2\mu_{nc}E_{nc}}/m_\pi$.

4.2 Mean square radii and geometry of 2n halo nuclei

The mean square radii for our three-body bound states are calculated from the matter density form factors in the low momentum transfer region. The matter density form factor is defined as the Fourier transform of the matter density:

$$\mathcal{F}(k^2) = \int \rho(\mathbf{x}) e^{i\mathbf{k}\cdot\mathbf{x}} d^3x, \quad (24)$$

with the normalization $\mathcal{F}(k^2 = 0) = 1$. In the low momentum transfer region, the exponential can be expanded, and assuming a spherically symmetric matter density, we see that the slope of the form factor determines the mean square radius $\langle r^2 \rangle$:

$$\begin{aligned} \mathcal{F}(k^2) &= \int \rho(\mathbf{x}) \left(1 + i\mathbf{k}\cdot\mathbf{x} - \frac{(\mathbf{k}\cdot\mathbf{x})^2}{2} + \dots \right) d^3x \\ &= 1 - \frac{1}{6}k^2\langle r^2 \rangle + \dots \end{aligned} \quad (25)$$

Of course, the mean square radius acquired depends on the choice of one- or two-body form factor. Since \mathbf{p} describes the relative momentum of the two particles in the two-body subsystem chosen, the slope of $\mathcal{F}_{ni}(k^2)$ will give the mean square distance between the two particles in the chosen two-body subsystem, either $\langle r_{nn}^2 \rangle$ or $\langle r_{nc}^2 \rangle$. Analogously, because \mathbf{q} describes the momentum of the spectator particle relative to the center of mass of the two-body subsystem, the slope of $\mathcal{F}_i(k^2)$, will give the mean square distance of the spectator particle from the center of mass of the two-body subsystem, either $\langle r_{c-nn}^2 \rangle$ or $\langle r_{c-nc}^2 \rangle$. However, it is more useful to calculate the distance of the individual particles from the center of mass of the three-body bound state. If b_i is the slope of the one-body form

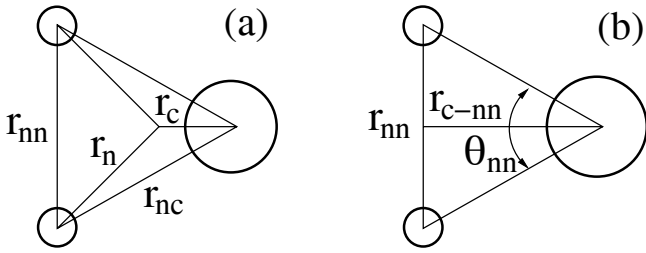


Fig. 6. (a) The various radii of the three-body system. (b) Further geometry of the $2n$ halo nucleus, specifically looking at the two-neutron opening angle θ_{nn} .

factor $\mathcal{F}_i(k^2)$ at the limit $k^2 = 0$, the mean square radius of one of the bodies i ($i = n, c$) from the three-body center of mass is given by

$$\langle r_i^2 \rangle = -6b_i \left(1 - \frac{m_i}{2m_n + m_c} \right)^2, \quad (26)$$

where m_i is the mass of the desired particle i , and m_n and m_c are the neutron and core masses, respectively. The various radii of the three-body system are illustrated in fig. 6(a).

We have extracted the radii by fitting a polynomial in k^2 to the form factor results for small k^2 . We have used polynomials of varying degree up to 5th order in k^2 in order to verify the stability and convergence of the fit. We have found a satisfactory stability in the slope when fitting to a polynomial to the fourth order in k^2 , up to a value of k^2 at which the form factor has dropped less than 10 percent.

As with the binding energies in the sequence of three-body Efimov states as discussed in sect. 3.1, the mean square radii of these states also display universal properties that are insensitive to the details of the two-body potential at short distances. One such property is that for the resonant limit, $a \rightarrow \pm\infty$, at which there are infinitely many arbitrarily shallow three-body bound states, the ratio of the radii of neighboring states approaches a universal factor as the threshold is approached. This universal scaling factor is exactly the inverse of the universal scaling factor found for the ratio of binding energies (see eq. (16)):

$$\langle r^2 \rangle^{(n)} / \langle r^2 \rangle^{(n+1)} \longrightarrow (\lambda_0)^{-2}, \quad (27)$$

as $n \rightarrow +\infty$ with $a = \pm\infty$. Therefore, we can construct a dimensionless quantity from the root of the product of the mean square radius and the three-body binding energy, $\sqrt{\langle r^2 \rangle B_3}$. The ratio of this quantity for neighboring states approaches unity in the resonant limit as the threshold is approached.

The extracted radii for known halo nuclei are shown in table 1. As input we have used the standard value of the n - n scattering length, $a_{nn} = (-18.7 \pm 0.6)$ fm [31], to calculate the n - n two-body virtual energy, $E_{nn} = 116.04$ keV, along with the experimental values of the n - c two-body energies, E_{nc} , shown in the third column of table 1 (negative values correspond to virtual energies). As a three-body input, the cutoff is tuned to reproduce the experimental

ground-state binding energy, $B_3^{(0)}$, shown in the second column of table 1. These experimental values for the two-body and three-body energies are taken from the most recent results of the ‘‘Nuclear Data Evaluation Project’’ of TUNL [30], except where otherwise noted. In the last column, we have given the experimental values for the n - n mean square radius, as given by Marqu es *et al.* [36]. These experimental values for $\sqrt{\langle r_{nn}^2 \rangle}$ were found using the three-body correlation study in the dissociation of two neutrons in halo nuclei, along with the two-neutron correlation function. However, the large uncertainty in these values is indicative of the need for more precise measurements of the mean square distances in $2n$ halo nuclei.

Our results agree overall with the study done by Yamashita *et al.* using a similar three-body model [37]. Our study expands on this previous work by showing the leading-order theoretical uncertainty as well as the results for an excited Efimov state in the case of ^{20}C .

The leading-order theoretical error is again estimated by the uncertainty of the two-body effective potential, eq. (2), which is $\approx r_0/a$, where r_0 is the effective range of the interaction, and a the scattering length. Using the inverse of the pion mass to estimate the effective range, $r_0 \approx 1/m_\pi$, the uncertainty in the radii is then calculated from the greatest of the errors arising from the n - n or n - c interaction: $\sqrt{2\mu_{nc}E_{nc}}/m_\pi$ or $\sqrt{2\mu_{nn}E_{nn}}/m_\pi$.

We will now discuss the results for the various known three-body halo nuclei as shown in table 1.

For ^{11}Li , there is a relatively large uncertainty in the experimental values of both the ground-state energy, $B_3^{(0)} = (247 \pm 80)$ keV [30], and the n - c virtual energy, with two competing values: $E_{nc} = (-25 \pm 15)$ keV [30], and $E_{nc} = (-800 \pm 250)$ keV [38]. For this reason it is advantageous to plot the various mean square radii over the full range of potential E_{nc} values. The results, using the central value for the three-body binding energy as input, $B_3^{(0)} = 247$ keV, can be seen in fig. 7, with error bands estimated from the theoretical uncertainty, as described above. These plots are a good general example of the relation between the mean square radii and the virtual two-body n - c energy for *Borromean* halo nuclei, where none of the two-body subsystems are bound. As the n - c virtual energy decreases in magnitude the three-body bound state increases slowly in size, with a more rapid increase in size as the energy approaches zero and crosses over into the *Samba* configuration, where the n - c subsystem becomes bound.

In table 1, we have highlighted, using the central value of the three-body binding energy, the central values of the competing n - c energies. While the two-body virtual energy reported in [38], $E_{nc} = -800$ keV, leads to $\sqrt{\langle r_{nn}^2 \rangle} = (6.8 \pm 1.8)$ fm in close agreement with the experimental result $\sqrt{\langle r_{nn}^2 \rangle}_{exp} = (6.6 \pm 1.5)$ fm a definite conclusion can not be reached due to the large error bars of the radii. We have also listed the upper and lower limits of the three-body binding energy, $B_3^{(0)} = 170$ and 320 keV, along with our preferred value of $E_{nc} = -800$ keV, which shows a more general result: for halo nuclei, the larger the three-

Table 1. Various mean square radii of different halo nuclei. The second two columns show the input values for the three-body ground state energy and the two-body n - c energy (negative values corresponding to virtual energies), respectively, as given by [30], except where otherwise noted. The experimental values for the n - n root mean square radii, shown in the last column, are taken from [36]. The rows marked by $^{20}\text{C}^*$ show the results for the excited Efimov state of ^{20}C , with binding energy displayed in the second column, which is found above the ground state ($B_3 = 3506$ keV).

Nucleus	B_3 [keV]	E_{nc} [keV]	$\sqrt{\langle r_{nn}^2 \rangle}$ [fm]	$\sqrt{\langle r_{nc}^2 \rangle}$ [fm]	$\sqrt{\langle r_n^2 \rangle}$ [fm]	$\sqrt{\langle r_c^2 \rangle}$ [fm]	$\sqrt{\langle r_{nn}^2 \rangle}_{exp}$ [fm]
^{11}Li	247	-25	8.7 ± 0.7	7.1 ± 0.5	6.5 ± 0.5	1.0 ± 0.1	6.6 ± 1.5
	247	-800 [38]	6.8 ± 1.8	5.9 ± 1.5	5.3 ± 1.4	0.9 ± 0.2	
	320	-800 [38]	6.2 ± 1.6	5.3 ± 1.4	4.8 ± 1.3	0.8 ± 0.2	
	170	-800 [38]	7.9 ± 2.1	6.7 ± 1.8	6.0 ± 1.6	1.0 ± 0.3	
^{14}Be	1120	-200 [39]	4.1 ± 0.5	3.5 ± 0.5	3.2 ± 0.4	0.40 ± 0.05	5.4 ± 1.0
^{12}Be	3673	503	3.0 ± 0.6	2.5 ± 0.5	2.3 ± 0.5	0.32 ± 0.07	
^{18}C	4940	731	2.6 ± 0.7	2.2 ± 0.6	2.1 ± 0.5	0.18 ± 0.05	
^{20}C	3506	161	2.8 ± 0.3	2.4 ± 0.3	2.3 ± 0.3	0.19 ± 0.02	
	3506	60	2.8 ± 0.2	2.3 ± 0.2	2.2 ± 0.2	0.18 ± 0.01	
	3506	0.0	2.7 ± 0.2	2.2 ± 0.2	2.1 ± 0.2	0.18 ± 0.01	
$^{20}\text{C}^*$	65.0 ± 6.8	60	42 ± 3	38 ± 3	41 ± 3	2.2 ± 0.2	
$^{20}\text{C}^*$	1.02 ± 0.08	0.0	130 ± 10	97 ± 7	93 ± 7	6.9 ± 0.5	

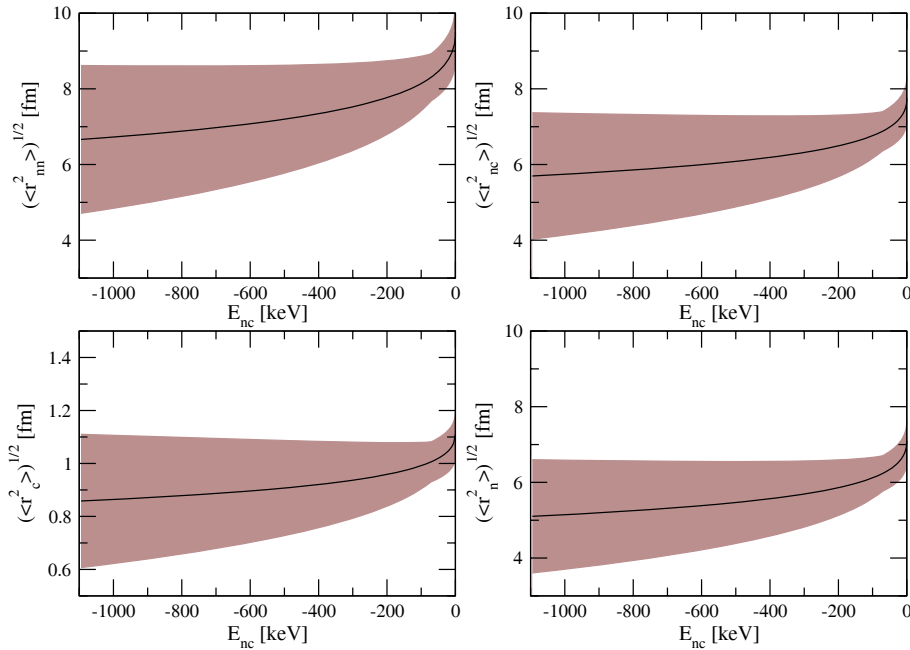


Fig. 7. The various mean square radii for ^{11}Li as a function of the n - ^9Li two-body energy (negative values correspond to the virtual state) with error bands from the theoretical uncertainty. As input, the n - n two body energy $E_{nn} = -116.04$ keV, and the three-body binding energy $B_3^{(0)} = 247$ keV were used.

body binding energy, the smaller the mean square radii. In terms of the plots in fig. 7, using a larger (smaller) value for $B_3^{(0)}$ as input would shift the curve down (up) in each plot. Due to the large uncertainties in both the theoretical and experimental values for ^{11}Li , there exists a large range of E_{nc} values which would produce a $\sqrt{\langle r_{nn}^2 \rangle}$ value in agreement with the experimental value of Marqués *et al.* [36].

As another example of a *Borromean* halo nucleus, we see that the calculated result for the n - n mean square radius of ^{14}Be , $\sqrt{\langle r_{nn}^2 \rangle} = (4.1 \pm 0.5)$ fm is smaller than the experimental value $\sqrt{\langle r_{nn}^2 \rangle}_{exp} = (5.4 \pm 1.0)$ fm [36], but still within one error bar. Here we have used the central value of the two-body n - c virtual energy as reported by [39], $E_{nc} = -200$ keV. In using the resonant limit, $E_{nc} = 0.0$ keV, we see that the largest theoretical value

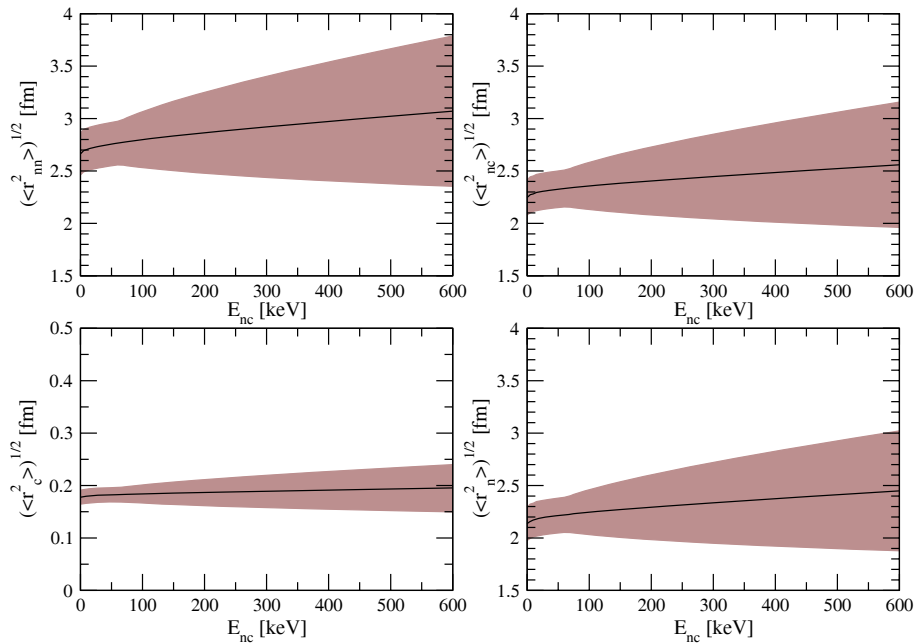


Fig. 8. The various mean square radii for ^{20}C as a function of the n - ^{18}C two-body energy with error bands from the theoretical uncertainty. As input, the n - n two-body energy $E_{nn} = -116.04$ keV, and the three-body binding energy $B_3^{(0)} = 3506$ keV were used.

for $\sqrt{\langle r_{nn}^2 \rangle} = (4.6 \pm 0.3)$ fm, which allows an unbound n - c two-body subsystem, is still smaller than the experimental value. Another reported value for the two-body virtual energy, $E_{nc} = (-1900 \pm 500)$ keV [30], would produce even smaller mean square radii, even farther away from the experimental value.

We now turn our attention to the so-called *Samba* halo nuclei in which the n - c subsystem is bound. As examples, we have listed the results for ^{12}Be and ^{18}C , using the central values of the experimental energies [30] in table 1.

Of greater interest are the results from the case of ^{20}C , as the large uncertainty in the n - c energy, with two competing values, $E_{nc} = (162 \pm 112)$ keV [30], and $E_{nc} = (530 \pm 130)$ keV [40], suggests that we look at the mean square radii over a range of E_{nc} values. The results, using the central value for the three-body binding energy as input, $B_3^{(0)} = 3506$ keV, can be seen in fig. 8, with error bands estimated from the theoretical uncertainty, as described above. These plots are a good general example of the relation between the mean square radii and the two-body n - c binding energy for *Samba* halo nuclei. As the n - c binding energy decreases in magnitude the three-body bound state decreases slowly in size, with a slightly more rapid decrease in size as the energy approaches zero and crosses over into the *Borromean* configuration, where the n - c subsystem becomes unbound. This suggests that as the two-body n - c state is more weakly bound, the particles must be closer together in order for the three-body state to be bound with the same energy.

As was shown in sect. 3.3, there possibly exists one Efimov excited state in ^{20}C for $E_{nc} < 165$ keV. The mean square radii for this excited state were calculated over a range of E_{nc} values and plotted, with leading-order error

bands, in fig. 9. Here we see the interesting phenomenon that although the radii remain relatively constant in the middle of the range of n - c energies which allow the excited state, as the endpoints are approached, the radii begin to increase rapidly, and then to diverge, both when $E_{nc} \rightarrow 165$ and $\rightarrow 0.0$ keV. It is at these points that the ^{20}C system moves outside the boundary curve depicted in fig. 3, the Efimov excited state is destroyed, and the three particles consequently fly apart.

In table 1, we have highlighted the result using the central value of the accepted n - c two-body binding energy, as well as two values which lead to an Efimov excited state, including the resonant limit $E_{nc} = 0.0$ keV. The rows marked by $^{20}\text{C}^*$ represent the results of the Efimov excited state. The three-body binding energy of this excited state is listed in the second column with leading-order theoretical uncertainty calculated as described in sect. 3.3.

Next we looked at a further geometrical property of $2n$ halo nuclei, specifically the two-neutron opening angle. As defined in fig. 6(b), it is straightforward to calculate θ_{nn} using the pair of mean square radii found from the three-body wave function Ψ_c , $\sqrt{\langle r_{nn}^2 \rangle}$ and $\sqrt{\langle r_{c-nn}^2 \rangle}$:

$$\tan\left(\frac{\theta_{nn}}{2}\right) = \frac{\frac{1}{2}\sqrt{\langle r_{nn}^2 \rangle}}{\sqrt{\langle r_{c-nn}^2 \rangle}}. \quad (28)$$

Our results for known halo nuclei are shown in table 2 using the central values of the experimental two-body and three-body energies as inputs (compare with table 1). We show the results for the competing values of the n - c virtual energy for the case of ^{11}Li . For the case of ^{20}C we also show the result with $E_{nc} = 0.0$ keV, along with its

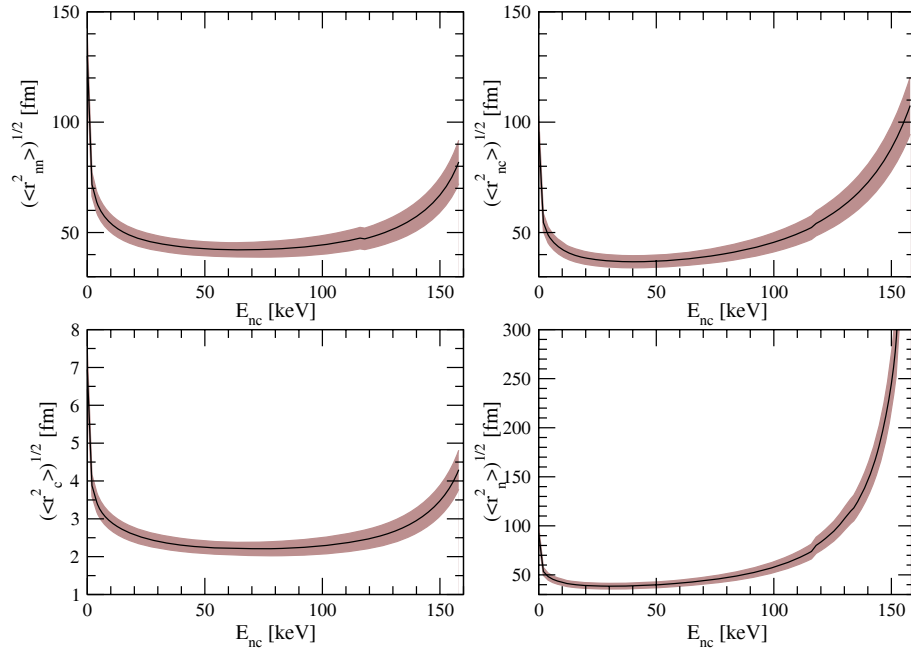


Fig. 9. The various mean square radii for the Efimov excited state of ^{20}C as a function of the n - ^{18}C two-body energy with error bands from the theoretical uncertainty. As input, the n - n two-body energy $E_{nn} = -116.04$ keV, and the three-body binding energy $B_3^{(0)} = 3506$ keV were used.

Table 2. Various two-neutron opening angles of different $2n$ halo nuclei calculated from the results for the mean square radii shown. They are compared with results of [41] and [42] shown in the last two columns, respectively.

Nucleus	$\sqrt{\langle r_{nn}^2 \rangle}$ [fm]	$\sqrt{\langle r_{c-nn}^2 \rangle}$ [fm]	θ_{nn}	θ_{nn} [41]	θ_{nn} [42]
^{11}Li	8.7 ± 0.7	5.5 ± 0.4	77_{-9}^{+8}	58_{-14}^{+10}	$56.2_{-21.3}^{+17.8}$
	6.8 ± 1.8	5.0 ± 1.3	68_{-25}^{+31}	66_{-18}^{+22}	$65.2_{-13.0}^{+11.4}$ [65.29]
^{14}Be	4.1 ± 0.5	2.8 ± 0.4	72_{-13}^{+16}	64_{-10}^{+9}	
^{12}Be	3.0 ± 0.6	1.9 ± 0.4	77_{-22}^{+23}		
^{18}C	2.6 ± 0.7	1.6 ± 0.4	78_{-27}^{+30}		
^{20}C	2.8 ± 0.3	2.0 ± 0.2	70_{-11}^{+11}		
	2.7 ± 0.2	1.8 ± 0.1	74_{-7}^{+7}		
$^{20}\text{C}^*$	130 ± 10	69 ± 5	87_{-9}^{+8}		

corresponding Efimov excited state. The opening angle has been calculated from experimental data in two recent works by Bertulani *et al.* [41], and Hagino *et al.* [42], and their results are shown in the last two columns, respectively. The study by Bertulani *et al.* uses the experimental values of $\sqrt{\langle r_{nn}^2 \rangle}$ found by Marqués *et al.* [36] seen in the last column of table 1, along with two different determinations of $\sqrt{\langle r_{c-nn}^2 \rangle}$ (see [41] and references within): using laser spectroscopy data (results displayed in the first row for ^{11}Li and ^{14}Be), and also using the $B(E1)$ strength (second row for ^{11}Li). However the result for ^{14}Be also uses a theoretical calculation for one of the inputs, rather than being a pure experimental result. On

the other hand, the study by Hagino *et al.* uses the experimental values of $B(E1)$ to calculate $\sqrt{\langle r_{c-nn}^2 \rangle}$, along with two different determinations of $\sqrt{\langle r_{nn}^2 \rangle}$ (see [42] and references within): using experimental values of the nuclear matter radii (first row for ^{11}Li), and using the results of Marqués *et al.* [36] (second row for ^{11}Li). Also, results found using a three-body model with density-dependent two-body contact interactions were found in [42], and are displayed in the third row for ^{11}Li . As would be expected, our results agree very well with the results from the three-body theoretical model used in [42]. Our result for ^{11}Li using our preferred choice of $E_{nc} = -800$ keV, also agrees very well with the experimental results obtained using the

value for $\sqrt{\langle r_{nn}^2 \rangle_{exp}}$ from Marqués *et al.*, which would be expected as our $\sqrt{\langle r_{nn}^2 \rangle}$ value also agrees with this experimental value. Overall there is a good agreement between our calculated results and the results of [41] and [42], as all θ_{nn} values lie within one error bar of each other. However, the size of these error bars suggest that further study should be done to improve both the experimental and theoretical results.

5 Conclusion

In this paper, we have investigated universal aspects of three-body halo nuclei within an effective quantum mechanics approach. Assuming that the halo nuclei have resonant S -wave interactions between the neutron and the core, the effective potential at leading order reduces to a separable S -wave potential. The corrections at next-to- and next-to-next-to-leading order in the expansion in M_{low}/M_{high} are determined by the S -wave effective ranges [43,44]. Corrections from P -wave interactions appear at even higher orders [4]. An important improvement compared to previous calculations is the inclusion of error bands based on the omitted higher-order terms in the effective theory.

We have calculated the parametric region within which at least one excited Efimov state will occur for different values of the core mass A . The boundary of this region is given by a curve in the plane described by the root of the ratio of the two-body bound (virtual) state energies to the ground-state energy [19]. We have calculated the boundary of this region for various values of the core mass A and provided error bands for the boundary curves. From the current experimental data, we conclude that none of the known halo nuclei is likely to have an excited Efimov state. One possible exception is ^{20}C which could have one excited state with a binding energy of less than 7 keV.

Next, we have studied the structure of known $2n$ halo nuclei, calculating the one- and two-body matter density form factors. From these form factors we were able to extract the mean square distances between the two particles in the chosen two-body subsystem, as well as the mean square distance of the spectator particle from the center of mass. We found that our results for the n - n mean square radius agree well with the experimental data for the *Borromean* halo nuclei ^{11}Li and ^{14}Be [36]. We have explicitly not studied the case of ^6He , which is dominated by a P -wave resonance in the n - c interaction (^5He) and requires a different counting scheme. While various schemes to treat such P -wave resonances in effective field theory have been developed [12,13], their application to three-body systems remains to be worked out. To the expected accuracy, our effective theory gives a good description of the studied halo nuclei. Using our results for the mean square distances, we have also calculated the two-neutron opening angle, and found a good general agreement with the recent results of [41] and [42].

Throughout this work we have estimated the theoretical error of the leading-order effective potential, eq. (2).

This uncertainty was quantified in our results through error bands. A future study could systematically improve the theoretical error through the inclusion of a momentum-dependent next-to-leading-order term in the effective potential which can be matched to the effective range of the interactions.

Another interesting application of this effective theory will be the study of Coulomb excitation data from existing and future facilities with exotic beams (such as FAIR and FRIB). In these experiments a nuclear beam scatters off the Coulomb field of a heavy nucleus. Such processes can populate excited states of the projectile which subsequently decay, leading to its ‘‘Coulomb dissociation’’ [45]. Effective theories offer a systematic framework for a full quantum-mechanical treatment of these reactions. In summary, with new improved experimental data for these weakly bound nuclei, much more knowledge can be obtained about the structure of these interesting systems as well as discovering whether they show universal behavior and excited Efimov states.

We thank L. Platter and A. Nogga for helpful discussions and U. Meißner for comments on the manuscript. This research was supported by the BMBF under contract number 06BN411.

Appendix A. Reconstruction of the wave function

In this section we give the expressions for the S -wave part of the full wave functions $\Psi_n(p, q)$ and $\Psi_c(p, q)$ where the index $i = n, c$ labels the chosen spectator particle. In the wave functions, the p Jacobi momentum describes the relative momentum between the two particles in the chosen two-body subsystem, while q describes the momentum of the spectator particle relative to the center of mass of the two-body subsystem.

For the neutron as the spectator particle, we find:

$$\begin{aligned} \Psi_n(p, q) = & G_0^n(p, q; B_3)g(p)t_n(q; B_3)F_n(q) \\ & + \frac{1}{2} \int_{-1}^1 dx [G_0^n(\tilde{\pi}_{nn}, \tilde{\pi}'_{nn}; B_3) \\ & \times g(\tilde{\pi}_{nn})t_n(\tilde{\pi}'_{nn}; B_3)F_n(\tilde{\pi}'_{nn})] \\ & + \frac{1}{2} \int_{-1}^1 dx [G_0^c(\tilde{\pi}_{nc}, \tilde{\pi}'_{nc}; B_3) \\ & \times g(\tilde{\pi}_{nc})t_c(\tilde{\pi}'_{nc}; B_3)F_c(\tilde{\pi}'_{nc})], \end{aligned} \quad (\text{A.1})$$

where the regulator function g and the T -matrices t_n and t_c are given in eqs. (3), (11), (13). The expressions for the propagators G_0^n and G_0^c can be found in eqs. (9) and (10). One can show through a simple substitution that $G_0^n(\tilde{\pi}_{nn}, \tilde{\pi}'_{nn}; B_3) = G_0^n(p, q; B_3)$, and $G_0^c(\tilde{\pi}_{nc}, \tilde{\pi}'_{nc}; B_3) = G_0^n(p, q; B_3)$, and the propagators simplify. Finally, the

shifted momenta are:

$$\begin{aligned}\tilde{\pi}_{nn} &\equiv \tilde{\pi}'_{nn}(p, q) \\ &= \sqrt{\frac{1}{(A+1)^2}p^2 + \frac{A^2(A+2)^2}{(A+1)^4}q^2 + \frac{A(A+2)}{(A+1)^3}2pqx},\end{aligned}\quad (\text{A.2})$$

$$\tilde{\pi}'_{nn} \equiv \tilde{\pi}'_{nn}(p, q) = \sqrt{p^2 + \frac{1}{(A+1)^2}q^2 - \frac{1}{A+1}2pqx}, \quad (\text{A.3})$$

$$\tilde{\pi}_{nc} \equiv \tilde{\pi}_{nc}(p, q) = \sqrt{\frac{1}{4}p^2 + \frac{(A+2)^2}{4(A+1)^2}q^2 + \frac{A+2}{2(A+1)}pqx}, \quad (\text{A.4})$$

$$\tilde{\pi}'_{nc} \equiv \tilde{\pi}'_{nc}(p, q) = \sqrt{p^2 + \frac{A^2}{(A+1)^2}q^2 - \frac{A}{A+1}2pqx}. \quad (\text{A.5})$$

If the core is the spectator particle, we find:

$$\begin{aligned}\Psi_c(p, q) &= \int_{-1}^1 dx [G_0^n(\tilde{\pi}_{cn}, \tilde{\pi}'_{cn}; B_3)g(\tilde{\pi}_{cn}) \\ &\quad \times t_n(\tilde{\pi}'_{cn}; B_3)F_n(\tilde{\pi}'_{cn})] \\ &\quad + G_0^c(p, q; B_3)g(p)t_c(q; B_3)F_c(q).\end{aligned}\quad (\text{A.6})$$

Again, one can show through a simple substitution that $G_0^n(\tilde{\pi}_{cn}, \tilde{\pi}'_{cn}; B_3) = G_0^c(p, q; B_3)$. For this case, the shifted momenta are given by

$$\begin{aligned}\tilde{\pi}_{cn} &\equiv \tilde{\pi}_{cn}(p, q) \\ &= \sqrt{\frac{A^2}{(A+1)^2}p^2 + \frac{(A+2)^2}{4(A+1)^2}q^2 + \frac{A(A+2)}{2(A+1)^2}2pqx},\end{aligned}\quad (\text{A.7})$$

$$\tilde{\pi}'_{cn} \equiv \tilde{\pi}'_{cn}(p, q) = \sqrt{p^2 + \frac{1}{4}q^2 - pqx}. \quad (\text{A.8})$$

Note Added in Proofs: After acceptance of this manuscript, we became aware that the experimental n - n radii from ref. [36] have to be interpreted with care. For more details on this issue, see ref. [46].

References

1. E. Braaten, H.-W. Hammer, Phys. Rep. **428**, 259 (2006) [arXiv:cond-mat/0410417].
2. P.F. Bedaque, H.-W. Hammer, U. van Kolck, Phys. Rev. Lett. **82**, 463 (1999) [arXiv:nucl-th/9809025]; Nucl. Phys. A **646**, 444 (1999) [arXiv:nucl-th/9811046].
3. V. Efimov, Phys. Lett. B **33**, 563 (1970).
4. P.F. Bedaque, U. van Kolck, Annu. Rev. Nucl. Part. Sci. **52**, 339 (2002) [arXiv:nucl-th/0203055].
5. P.F. Bedaque, G. Rupak, H.W. Griesshammer, H.-W. Hammer, Nucl. Phys. A **714**, 589 (2003) [arXiv:nucl-th/0207034].
6. L. Platter, H.-W. Hammer, U.-G. Meißner, Phys. Lett. B **607**, 254 (2005) [arXiv:nucl-th/0409040].
7. K. Riisager, Rev. Mod. Phys. **66**, 1105 (1994).
8. M.V. Zhukov, B.V. Danilin, D.V. Fedorov, J.M. Bang, I.J. Thompson, J.S. Vaagen, Phys. Rep. **231**, 151 (1993).
9. P.G. Hansen, A.S. Jensen, B. Jonson, Annu. Rev. Nucl. Part. Sci. **45**, 591 (1995).
10. I. Tanihata, J. Phys. G **22**, 157 (1996).
11. A.S. Jensen, K. Riisager, D.V. Fedorov, E. Garrido, Rev. Mod. Phys. **76**, 215 (2004).
12. C.A. Bertulani, H.-W. Hammer, U. Van Kolck, Nucl. Phys. A **712**, 37 (2002) [arXiv:nucl-th/0205063].
13. P.F. Bedaque, H.-W. Hammer, U. van Kolck, Phys. Lett. B **569**, 159 (2003) [arXiv:nucl-th/0304007].
14. C.A. Bertulani, R. Higa, U. van Kolck, in preparation.
15. R. Higa, H.-W. Hammer, U. van Kolck, Nucl. Phys. A (in press) [arXiv:0802.3426 [nucl-th]].
16. H.-W. Hammer, R. Higa, Eur. Phys. J. A **37**, 193 (2008) [arXiv:0804.4643 [nucl-th]].
17. T. Kraemer *et al.*, Nature **440**, 315 (2006) [arXiv:cond-mat/0512394v2].
18. D.V. Fedorov, A.S. Jensen, K. Riisager, Phys. Rev. Lett. **73**, 2817 (1994) [arXiv:nucl-th/9409018].
19. A.E.A. Amorim, T. Frederico, L. Tomio, Phys. Rev. C **56**, R2378 (1997) [arXiv:nucl-th/9708023].
20. I. Mazumdar, V. Arora, V.S. Bhasin, Phys. Rev. C **61**, R051303 (2000).
21. L. Platter, H.-W. Hammer, U.-G. Meißner, Phys. Rev. A **70**, 052101 (2004) [arXiv:cond-mat/0404313].
22. L. Platter, H.-W. Hammer, U.-G. Meißner, Few Body Syst. **35**, 169 (2004) [arXiv:cond-mat/0405660].
23. V.F. Kharchenko, Sov. J. Nucl. Phys. **16**, 173 (1973) [Yad. Fiz. **16**, 310 (1972)].
24. V. Efimov, Comments Nucl. Part. Phys. **19**, 271 (1990).
25. L.H. Thomas, Phys. Rev. **47**, 903 (1935).
26. S.K. Adhikari, A. Delfino, T. Frederico, I.D. Goldman, L. Tomio, Phys. Rev. A **37**, 3666 (1988).
27. F. Robicheaux, Phys. Rev. A **60**, 1706 (1999).
28. M.T. Yamashita, T. Frederico, M.S. Hussein, Mod. Phys. Lett. A **21**, 1749 (2006) [arXiv:nucl-th/0501052].
29. E. Tiesinga, B.J. Verhaar, H.T.C. Stoof, Phys. Rev. A **47**, 4114 (1993).
30. TUNL nuclear data evaluation project. WWW: <http://www.tunl.duke.edu/NuclData/>.
31. D.E. Gonzales Trotter *et al.*, Phys. Rev. Lett. **83**, 3788 (1999).
32. G. Audi, A.H. Wapstra, Nucl. Phys. A **595**, 409 (1995).
33. M.T. Yamashita, T. Frederico, L. Tomio, Phys. Lett. B **660**, 339 (2008) [arXiv:0704.1461 [nucl-th]].
34. V. Arora, I. Mazumdar, V.S. Bhasin, Phys. Rev. C **69**, R061301 (2004).
35. I. Mazumdar, A.R.P. Rau, V.S. Bhasin, Phys. Rev. Lett. **97**, 062503 (2006) [arXiv:quant-ph/0607193].
36. F.M. Marqués *et al.*, Phys. Lett. B **476**, 219 (2000); Phys. Rev. C **64**, 061301 (2001).
37. M.T. Yamashita, L. Tomio, T. Frederico, Nucl. Phys. A **735**, 40 (2004) [arXiv:nucl-th/0401063].
38. K.H. Wilcox *et al.*, Phys. Lett. B **59**, 142 (1975).
39. M. Thoennessen, S. Yokoyama, P.G. Hansen, Phys. Rev. C **63**, 014308 (2000).

40. T. Nakamura *et al.*, Phys. Rev. Lett. **83**, 1112 (1999).
41. C.A. Bertulani, M.S. Hussein, Phys. Rev. C **76**, 051602 (2007) [arXiv:0705.3998 [nucl-th]].
42. K. Hagino, H. Sagawa, Phys. Rev. C **76**, 047302 (2007) [arXiv:0708.1543 [nucl-th]].
43. H.-W. Hammer, T. Mehen, Phys. Lett. B **516**, 353 (2001).
44. L. Platter, D.R. Phillips, Few Body Syst. **40**, 35 (2006).
45. C.A. Bertulani, G. Baur, Phys. Rep. **163**, 299 (1988).
46. N.A. Orr, arXiv:0803.0886.